Available online at www.sciencedirect.com
ScienceDirect
Journal of Power Sources 161 (2006) 920–928
JOURNAL OF POWER SOURCES
www.elsevier.com/locate/jpowsour

AC impedance diagnosis of a 500 W PEM fuel cell stack Part I: Stack impedance☆

Xiaozi Yuan[a], Jian Colin Sun[a], Mauricio Blanco[a,b], Haijiang Wang[a,*], Jiujun Zhang[a], David P. Wilkinson[a,b]

[a] *Institute for Fuel Cell Innovation, National Research Council Canada, Vancouver, BC, Canada V6T 1W5*
[b] *Department of Chemical and Biological Engineering, University of British Columbia, Vancouver, BC, Canada V6T 1Z4*

Received 16 March 2006; received in revised form 28 April 2006; accepted 3 May 2006
Available online 15 June 2006

Abstract

Diagnosis of stack performance is of importance to proton exchange membrane (PEM) fuel cell research. This paper presents the diagnostic testing results of a 500 W Ballard Mark V PEM fuel cell stack with an active area of 280 cm^2 by electrochemical impedance spectroscopy (EIS). The EIS was measured using a combination of a FuelCon test station, a TDI loadbank, and a Solartron 1260 Impedance/Gain-Phase Analyzer operating in the galvanostatic mode. The method described in this work can obtain the impedance spectra of fuel cells with a larger geometric surface area and power, which are normally difficult to measure due to the limitations on commercial load banks operating at high currents. By using this method, the effects of temperature, flow rate, and humidity on the stack impedance spectra were examined. The results of the electrochemical impedance analysis show that with increasing temperature, the charge transfer resistance decreases due to the slow oxygen reduction reaction (ORR) process at low temperature. If the stack is operated at a fixed air flow rate, a low frequency arc appears and grows with increasing current due to the shortage of air. The anode humidification cut-off does not affect the spectra compared to the cut-off for cathode humidification.

Keywords: AC impedance; Electrochemical impedance spectroscopy (EIS); Proton exchange membrane fuel cell (PEMFC); Stack

1. Introduction

There has been significant development in the potential use of proton exchange membrane (PEM) fuel cells for residential applications and electric vehicles. The performance of PEM fuel cell systems depends on a complex group of parameters. The most common method used to characterize the electrochemical performance of the fuel cell systems is to the examine current–voltage curves because this method is easier to implement than any other electrochemical technique, such as AC impedance and the current interruption method. Also, it reveals the different electrode processes occurring at different current density levels [1]. However, details of the underlying mechanisms are difficult to obtain by this method. Electrochemical impedance spectroscopy (EIS), also known as AC impedance, is a very useful method for the analysis of electrochemical systems. Due to the electrochemical nature of fuel cells, EIS has been demonstrated to be a powerful technique to study the fundamental processes in fuel cells [2]. The main advantage of EIS is its ability to distinguish, in the frequency domain, the individual contributions of the interfacial charge transfer resistance, and the mass transport resistances in the catalyst layer and backing diffusion layer [1]. The disadvantage of this method is that it does not generate local information unless significant complexity is added to the measurement set-up and there is a danger of drawing the wrong conclusions and obtaining inaccurate quantitative data because many different models can fit the same data.

EIS is usually measured using an electrochemical half-cell. From a practical point of view, the most interesting data are those from in situ fuel cell operation. The impedance spectrum of a fuel cell in operation is normally measured in the H_2/O_2 or H_2/air gas feed mode. It can provide information about the cathode and the anode impedance [3]. But it is known that the cathode impedance typically dominates the proton exchange membrane

☆ Partially presented at the 208th ECS conference.
* Corresponding author. Tel.: +1 604 221 3038; fax: +1 604 221 3001.
E-mail address: haijiang.wang@nrc.gc.ca (H. Wang).

0378-7753/$ – see front matter © 2006 Elsevier B.V. All rights reserved.
doi:10.1016/j.jpowsour.2006.05.003

fuel cell (PEMFC) impedance because the hydrogen oxidation reaction is much faster than the oxygen reduction reaction [4]. By changing the gas feed mode, e.g. H_2/H_2, O_2/O_2, and H_2/N_2, EIS information on a full cell in operation can be obtained. The EIS measurement can be operated in either potentiostatic mode or galvanostatic mode. The evaluation of the charge transfer resistances in the galvanostatic mode is preferred because it is the usual mode for fuel cell operation and it forces a constant conversion rate with respect to the charged species [5].

Since EIS was used to study porous gas diffusion electrodes at the beginning of the 1980s, the increasing challenge to fuel cell systems has resulted in a variety of EIS techniques to analyze the performance losses in fuel cells. EIS has been applied to the characterization of the PEM fuel cell with respect to many different parameters. Examples, reported in the literature, of the applications of EIS in fuel cell understanding, design, and operation are listed below:

- Optimization of the membrane electrode assembly (MEA) fabrication:
  - catalyst loading [6];
  - polytetrafluroethylene (PTFE) concentration [6];
  - Nafion loading [6–8];
  - composite electrode structure [9];
  - membrane thickness [10–12];
  - fabrication method [13–15].
- Optimization of operation conditions:
  - cell humidification [2,6,10,11,17–20];
  - temperature [11];
  - pressure and flow rate [21].
- Membrane resistance [22–28].
- Contamination [4,5,29–31].
- Fuel cell stack resistance [23,32].
- Localized EIS [33,34].

Although much effort has been made to diagnose the PEM fuel cell by applying EIS, most studies have focused on single cells. Only limited work has been done with fuel cell stacks, especially high power stacks with large active areas. On the one hand, dealing with a larger area fuel cell stack needs a high power test station and a heavy-duty load bank, which are very costly for researchers. On the other hand, most commercial load banks operating at high currents do not have good frequency responses [34]. However, the evaluation of high power stack performance is of importance for PEM fuel cell commercialization and for real applications. The main purpose of this study is to measure the electrochemical impedance spectra of a 500 W Ballard Mark V PEM fuel cell stack using a set-up that consists of a FuelCon test station, a TDI loadbank, and a Solartron 1260 Impedance/Gain-Phase Analyzer, and to further study, from the EIS measurement results, the effects of temperature, flow rate, and humidity on the performance of the fuel cell stack.

2. Experimental

The fuel cell stack tested in this work has six cells with an active area of 280 cm^2. The MEA consists of a Nafion 115 membrane with a total Pt catalyst loading of 1.0 mg cm^{-2}, and Toray TGP 090 gas diffusion layers. The experiments were conducted in the galvanostatic mode using a 500 W FuelCon Test Station and a water-cooled electronic load system from TDI (WCL 488400-1000-12000) that has a maximum current of 1000 A. The hydrogen and air flow rate were kept at a constant stoichiometry of 2 and 2.5, respectively, unless otherwise stated. Both the anode and cathode sides were kept at 100% relative humidity.

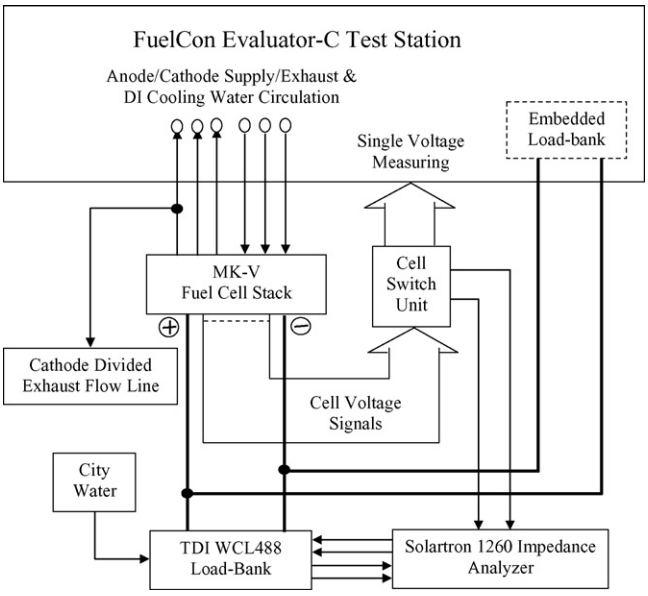

Fig. 1. Experimental schematic for the EIS measurement of the 500 W fuel cell stack.

There is a wide choice of instruments and techniques available for the measurement of EIS, ranging from a simple oscilloscope display to a Fast Fourier Transform (FFT) analyzer. In this work, the EIS measurement was carried out using a Solartron 1260 Impedance/Gain-Phase Analyzer, which is commonly used in impedance studies. The impedance spectra were recorded by sweeping frequencies over the range of 20 kHz–100 mHz with 10 points $decade^{-1}$. The amplitude of the AC current was always kept at 5% of the DC current [35,36] (the selection of the amplitude of AC current will be discussed in Part II of this study). The technical set-up of the testing facilities is depicted in Fig. 1.

Measuring an EIS spectrum takes time because the system must be at steady state throughout the measurement. A common problem in EIS measurements and subsequent analysis is the drifting of the system being measured. To achieve a steady-state environment before starting each impedance measurement, the fuel cell stack was operated at 100 A (individual cell potential is about 0.6 V) for at least 1 h until a steady-state voltage was obtained. The voltages before and after the EIS measurement were determined to verify the stability of the cell. In addition, during the EIS measurements only one variable was allowed to change while the other variables were kept constant for each measurement. This allows better understanding of the effects of each of the variables [16].

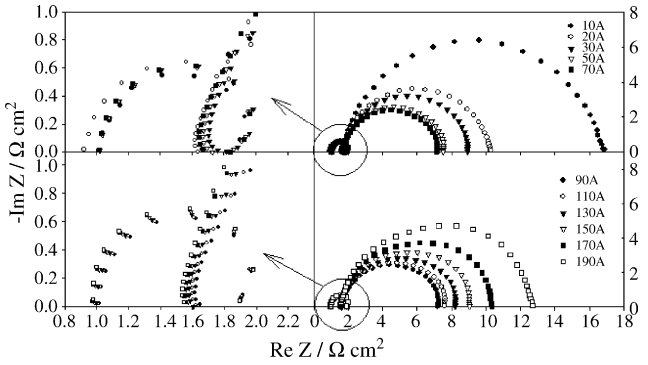

Fig. 2. Current dependence of the Nyquist plots over the range of 10–190 A at 30 °C.

3. Results and discussion

3.1. General pattern of the stack EIS

Typical impedance spectra measured at different currents or overpotentials are presented in Fig. 2. For clarity, the impedance loops in the Nyquist plot are described as high, medium, and low frequency loops, respectively, from high frequency to low frequency in the case of three loops. In case there are only two loops they are described as high and low frequency loops, respectively, according to the location of the frequency region.

Generally, at low currents (10–70 A) there are two characteristic semicircle loops seen in the spectra. The bigger loop (low frequency loop, from 1k Hz to 0.1 Hz) that changes with the current reflects the behavior of the PEMFC stack cathode. The loop is called the "kinetic loop" corresponding to the charge transfer process of the oxygen reduction reaction (ORR). Jaouen et al. [37,38] explained that the potential dependent loop is related to the double layer capacitance of the electrode combined with the charge transfer resistance of the ORR and, thus, the diameter of this loop is determined by the charge transfer resistance, whose dependence on electrode potential is given by the Tafel equation. A similar explanation can also be found in Paganin et al.'s study [39] through the interpretations of different models of the impedance response of a polymer electrolyte fuel cell.

The smaller semicircle (high frequency loop, from 2k Hz to 1k Hz) can be detected at different overpotentials or currents. This high frequency component has not been observed to vary very much with changing overpotential or current. Romero-Castanon et al. [40] reported that it is associated with the structural features of the MEAs. Freire and Gonzalez [11] have attributed the high frequency relaxation to distributed resistance effects in the electrolyte within the catalyst layer. Fischer et al. [41] have explained that the internal ohmic resistance and the contact capacitance in the granular electrode structure might be responsible for the high frequency loop.

In our measurement, the high frequency feature is strongly affected by the measurement circuit because in the high frequency region, from 1k Hz to 2k Hz, the load bank does not have an accurate response to the excitation. Valid and useful signals begin at around 1k Hz where the kinetic loop begins to develop. The kinetic loop can be easily identified by the dependence on current or current density. A knot between the low frequency loop and the high frequency loop is observed very possibly due to certain overlap of the two loops and the different frequency responses of the two loops. Fortunately, the overlap is just at the very beginning of the kinetic loop. There is clear distinction between the loops. The electrode process can therefore still be analyzed by the spectra without being affected by the high frequency "artefacts", which might be related to the fine structure of the fuel cell and deserve extensive studies by using equipments with a higher frequency response. In this paper the high frequency feature is excluded in the spectra but is still shown in different plots to provide the full picture of the measurement results. The Randles cell, depicted in Fig. 3a, was used to model the system to fit the spectra measured at low currents (10–70 A), excluding the high frequency part of the spectra.

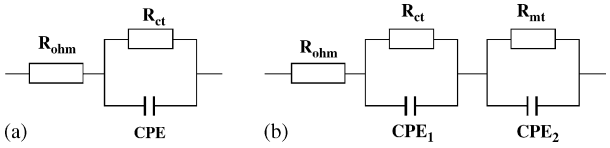

Fig. 3. Equivalent circuit of the stack—equivalent circuit for: (a) one loop and (b) two loops.

As shown in Fig. 3a, the high frequency (HF) intercept of the kinetic loop is generally related to the ohmic resistance of the stack, R_Ω. The diameter of the kinetic loop corresponds to the charge transfer resistance for the oxygen reduction reaction, R_{ct}, and constant phase element (CPE, defined as $Z(\mathrm{CPE}) = 1/Q(\mathrm{j}w)^{-n}$, where Q has the numerical value of the admittance ($1/|Z|$) at $\omega = 1\ \mathrm{rad\ s^{-1}}$ and n is the exponent value) represents the catalyst layer capacitance properties associated with the oxygen reduction reaction. The reason for replacing C by CPE results from the fact that the capacitance due to the double layer charging is distributed along the length of the pores in the porous electrode [42]. Fitting the data in Fig. 2 at low currents (up to 70 A) to this model results in a $0.24\ \Omega\ \mathrm{cm^2}$ value of R_Ω, which is quite acceptable according to the Nafion 115 membrane resistance. The value of n obtained is around 0.9. As seen in Fig. 2, the charge transfer resistance decreases with increasing current from 10 A to 70 A. In terms of equivalent circuits, the charge transfer resistance decreases from $15.1\ \Omega\ \mathrm{cm^2}$ to $5.6\ \Omega\ \mathrm{cm^2}$, resulting from the increasing driving force for the charge transfer reaction.

At high currents above 80 A, a distortion of the kinetic loops can be observed, which is well known to be the result of overlapping of two semicircles. One corresponds to the kinetic contribution and the other corresponds to mass transport. By contrast, at low currents the kinetic contribution dominates the cell performance. The mass transfer limitation at high currents can also be observed from the polarization curve at high current or current density. Thus, the equivalent circuit, as depicted in Fig. 3b, is more suitable for high currents above 80 A and it can fit the experimental data fairly well. In Fig. 3b, R_{ct} is the charge transfer resistance for the oxygen reduction, and $\mathrm{CPE_1}$ represents the R_{ct} associated catalyst layer capacitance properties. R_{mt} is the mass transfer resistance of oxygen in the catalyst layer and $\mathrm{CPE_2}$ represents the R_{mt} associated capacitance. As observed in Fig. 2, the

size of the distorted loop at high currents increases with current. Fitting of the spectra to the equivalent circuit model in Fig. 3b shows that from 90 A to 190 A, the charge transfer resistance increased from 4.2 Ω cm^2 to 9.1 Ω cm^2 and mass transfer resistance increased from 1.5 Ω cm^2 to 2.2 Ω cm^2. These results tell us that the equivalent circuit model in Fig. 3b still cannot account for the exact electrode process at high currents, because the charge transfer resistance obtained by this model is still increasing with increasing currents. The reason is most probably due to the complicated mass transport phenomenon in fuel cells in contrast to the case of solution electrochemistry with a planar electrode. In fuel cells, the mass transport in the flow channels, in the porous gas diffusion layer and catalyst layer, is very different. So it is possible that the equivalent circuit in Fig. 3b can account for only part of the mass transport contribution; therefore, the charge transfer resistance obtained still contains some mass transport component to make the charge transfer resistance a kind of effective charge transfer resistance and increase with currents. Similar phenomena have been reported previously [16].

On closer examination of the high frequency loops in Fig. 2, one can see that there are tiny differences in the loops and a change in high frequency intercept of the kinetic loop at different currents. As a matter of fact, the change of the high frequency intercept is complicated and affected by many factors, in particular, the water content in the membrane. The effect of current or overpotential on the high frequency loop intercept needs further investigation.

Fig. 4 shows the typical current dependence of the Bode plots on the experimental results shown in Fig. 2. Basically, two peaks are observed in the Bode plot and reflect the two loops in the Nyquist plot of Fig. 2. In the Bode plots, the mass transfer feature is not as accentuated as in the Nyquist plots since the mass transfer resistance is much smaller than the charge transfer resistance as shown by the model fitting results. Comparably, the charge transfer peak is reduced with increasing current, and the peak frequency increases with increasing current up to 80 A as seen in the Bode plots in Fig. 4. At high currents beyond 80 A, the effective charge transfer peak grows and the peak frequency decreases with increasing current. It is also seen that beyond 80 A the loop starts to grow again with current because an increase in effective charge transfer resistance at high current occurs due to the increasing mass transfer limitations [16].

The current dependence of the spectra at high currents results from the combination of conductivity and mass transport limitations within the catalyst layer. Springer et al. [16] have attributed the effective charge transfer resistance to the rate of interfacial oxygen reduction process. The protonic conductivity and oxygen permeability limitations within the catalyst layer also contribute to the charge transfer resistance. Freire and Gonzalez [11] suggested that the effect should be due to either oxygen or proton transport limitations. If this phenomenon were due to proton transport effects only, the high frequency region would be expected to end on a 45° straight line. Since a 45° straight line cannot be clearly defined, it must be concluded that the effect is due mainly to oxygen diffusion limitations in the catalyst layer.

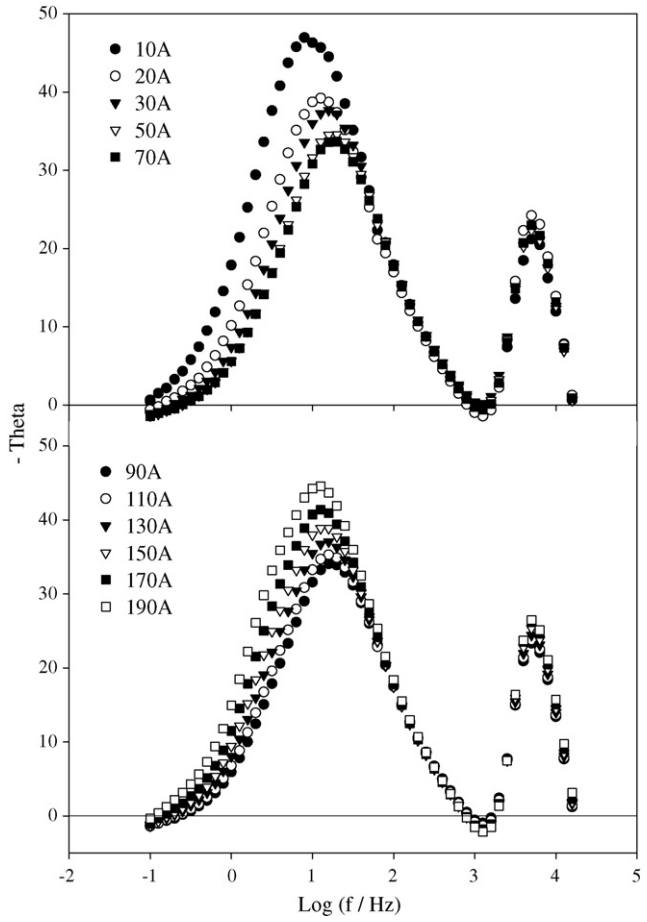

Fig. 4. Current dependence of the Bode plots over the range of 10–190 A at 30 °C.

3.2. Temperature effect

Fig. 5a and b shows the current dependence of Nyquist plots at 50 °C and 70 °C, respectively. The same current dependence trends observed in Fig. 2 are also observed here in Fig. 5a and b, i.e., with increasing current the diameter of the kinetic loop decreases at low currents, and after the current exceeds a certain value, the loop begins to distort and increase as the current increases due to mass transfer limitation. Fig. 5 indicates that the high frequency intercept of the kinetic loop changes with temperature; however, only tiny differences between the different currents were observed.

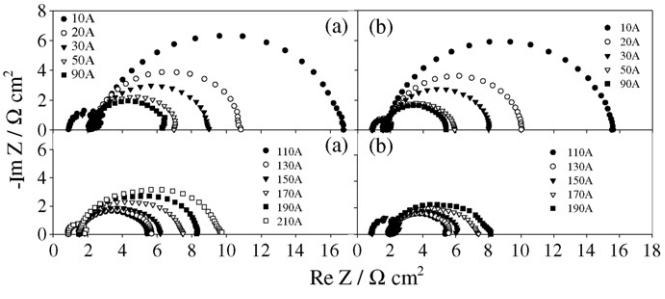

Fig. 5. Current dependence of the Nyquist plots at: (a) 50 °C and (b) 70 °C.

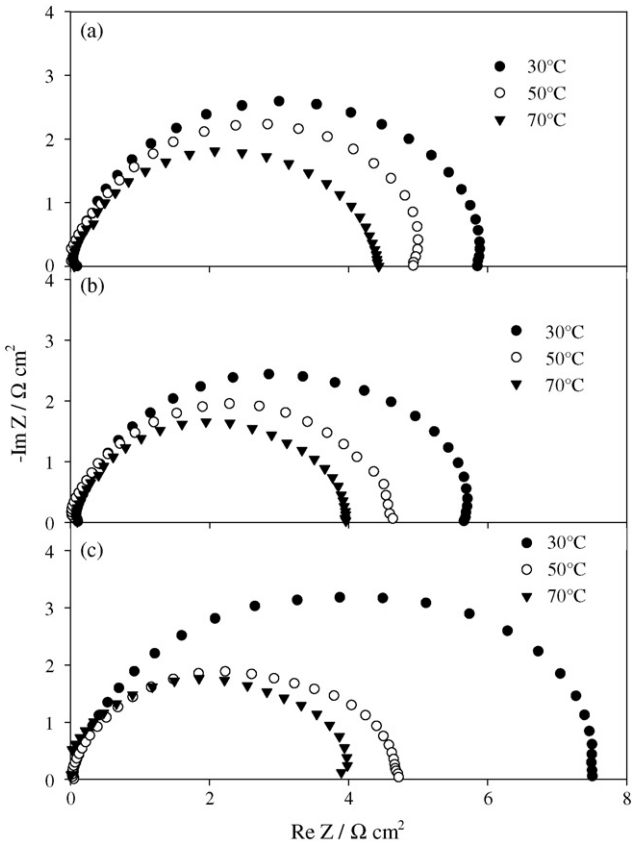

Fig. 6. Comparison of the IR-corrected Nyquist plots at different temperatures: (a) 50 A; (b) 100 A; (c) 150 A.

Fig. 6 shows the comparison of the Nyquist plots at different temperatures for different currents. In order to make a clearer comparison, Fig. 6 was corrected by the ohmic drop in the stack using the high frequency intercept of the kinetic loop. As seen in Fig. 6a–c, the diameter of the kinetic loop decreases as the temperature increases at the chosen currents of 50 A, 100 A, and 150 A, respectively. Because the performance of the fuel cell systems is severely limited by the slow oxygen electrode kinetics at low operating temperatures, the kinetic loop is larger at low temperatures than at high temperatures.

By fitting the kinetic loop with the equivalent circuits (shown in Fig. 3), the stack resistance and the maximum frequency of the kinetic loop can be obtained. The stack reaction resistance and peak frequency of the kinetic loop at different temperatures can be compared as shown in Figs. 7 and 8, respectively. Fig. 7 shows that with increasing temperature, the stack reaction resistance decreases at any current. Fig. 7 also shows the trend of the stack reaction resistance with change of current. In each case, the stack reaction resistance begins to increase above a certain current, i.e., about 70 A at 30 °C, 110 A at 50 °C, and 120 A at 70 °C. The onset current of the mass transfer effect increases with temperature attributes to the increasing effective mass transport at higher temperatures. Fig. 8 shows that with increasing temperature, the peak frequency increases and goes through a maximum with increase of current. By fitting the kinetic loop the variation trend of the peak frequency is nearly opposite to that of the charge transfer resistance as it appears in Fig. 8.

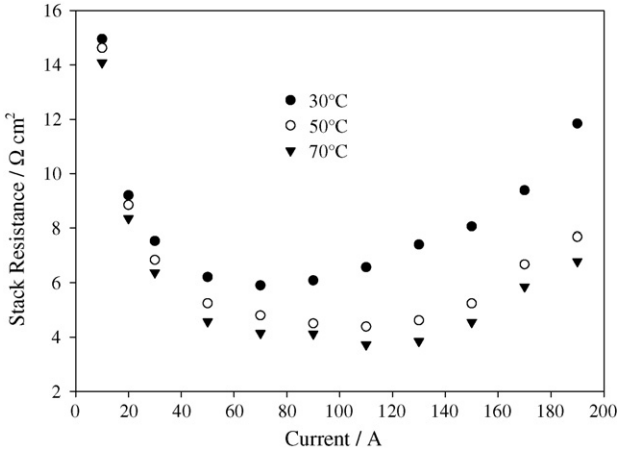

Fig. 7. Comparison of stack reaction resistance at different temperatures.

Also from Fig. 7, at 70 °C the average single cell resistance per unit area is approximately 8 mΩ, 5 mΩ, and 4 mΩ at currents of 10 A, 20 A, and 30 A, respectively. The values are calculated from the total resistances, the active area, and the number of cells. In Diard et al.'s [32] work, the single cell resistance per unit area is approximately 20 mΩ. Their measurements were carried out at 80 °C and 3 A in a four-cell stack with an active area of 24 cm^2. Comparing with 20 mΩ, the values obtained here are reasonable because the resistance will be larger at lower current. These results also approximately coincide with Springer et al.'s [16] classical spectra, although the cell being measured and the operation conditions are different. It indicates that the method described in this work is applicable.

3.3. Flow rate effect

Perry et al. [43] reported that at the higher current densities, which are required to achieve higher power, mass transport effects become more significant. However, mass transport limitations can be reduced by using different operating conditions such as higher reactant flow. Young et al. [21] operated a fuel cell at more than 20 times the stoichiometric flow rate, which is

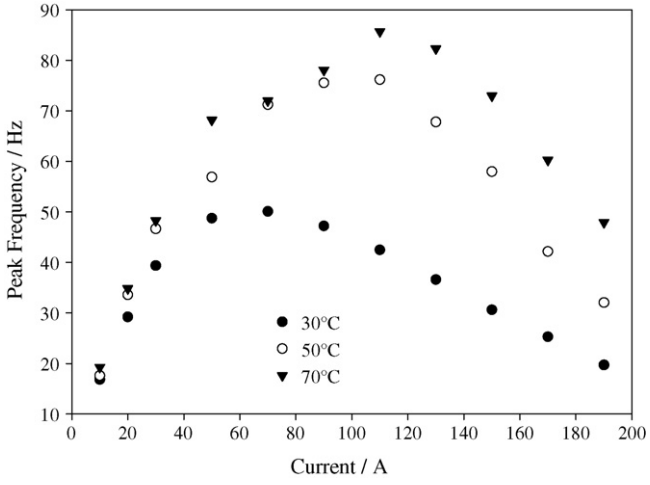

Fig. 8. Comparison of peak frequency at different temperatures.

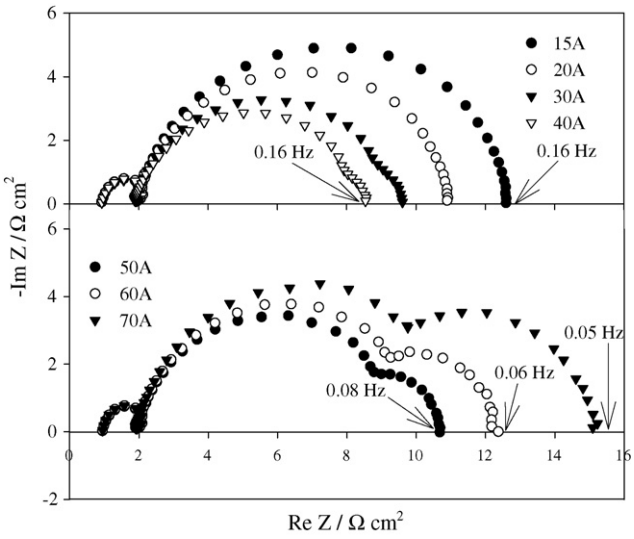

Fig. 9. Effect of air shortage on the Nyquist plots at 30 °C. The air flow rate was 20 L min^{-1}.

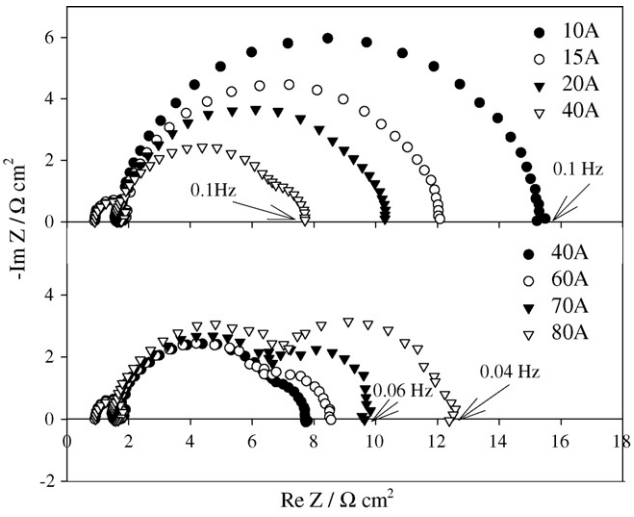

Fig. 10. Effect of air shortage on the Nyquist plots at 50 °C. The air flow rate was 20 L min^{-1}.

much higher than that usually employed in fuel cell operation, to eliminate mass transfer effects. Ciureanu [23] used a constant stoichiometry of 4 for the inlet air flow in order to ensure complete removal of the water produced in the cathode compartment. Comparison of impedance spectra at different reactant flow rates provides information about the effect of gas diffusion on mass transport and the different features of the impedance spectra, e.g. the low frequency (mass transfer) arc [4].

As discussed previously, only at high currents will the mass transfer feature show in the spectrum when the stack is operated with a hydrogen stoichiometry of 2, and an air flow stoichiometry of 2.5, and this mass transfer feature is almost masked by charge transfer. If the fuel cell stack is operated at a fixed air flow rate of 20 standard L min^{-1}, and a constant hydrogen stoichiometry of 2, even at low currents the impedance spectra of the stack operated will show a third low frequency arc. The effects of air shortage on the Nyquist plots at 30 °C and 50 °C are displayed in Figs. 9 and 10, respectively.

As shown in Fig. 9, at the current of 30 A, the third low frequency arc begins to grow at 30 °C. With increasing current, the low frequency arc becomes larger and larger. Seen from the Bode plots at 30 °C in Fig. 11, a third peak appears associated with the third arc in the Nyquist plots. Again, with increasing current, the third peak grows in Bode plots. Similar phenomenon can be observed at 50 °C. The low frequency arc begins to grow at about 20 A, as shown in Fig. 10. Fig. 12 clearly demonstrates the effect of air shortage on the Bode plots.

The third low frequency arc reflects the mass transport limitations in the gas phase because of the shortage of the air supply operated at a fixed air flow rate. Sometimes, a third arc appears as a straight line with a slope of 1 (45°, real part = imaginary part), which is considered to be the infinite diffusion control [3]. However, in the Nyquist diagram the limited diffusion as an additional loop at low frequency range is observed instead of the straight line seen in our experiments. There are some other explanations in the literature about this low frequency arc. Freire and Gonzalez [11] reported that this additional arc has two contributions: the effect of liquid water formed at the cathode, which affects the transport of oxygen, and the hydration effects that limit water transport in the membrane. Paganin et al. [39] reported that a low frequency relaxation process at high

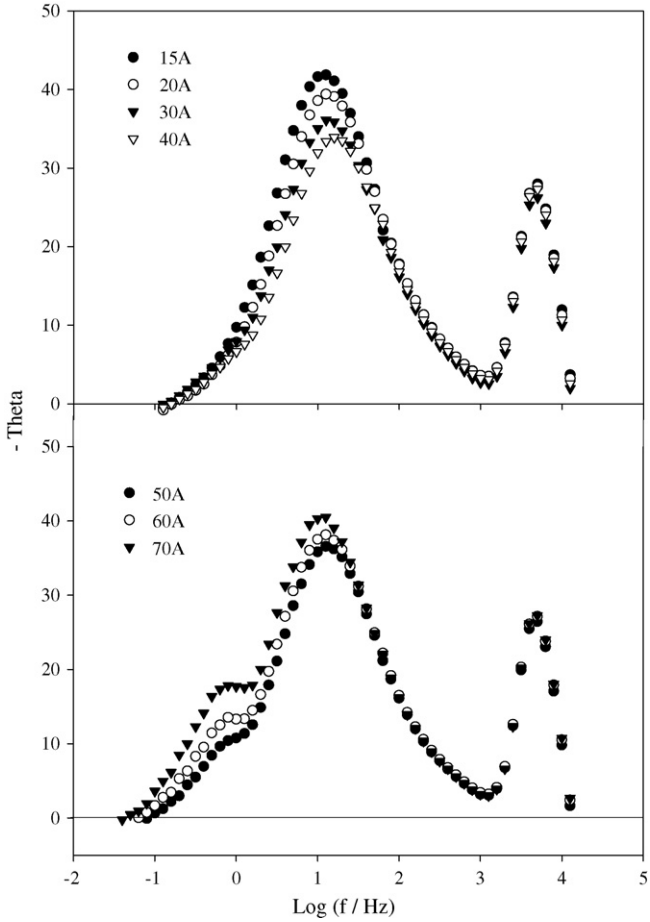

Fig. 11. Effect of air shortage on the Bode plots at 30 °C. The air flow rate was 20 L min^{-1}.

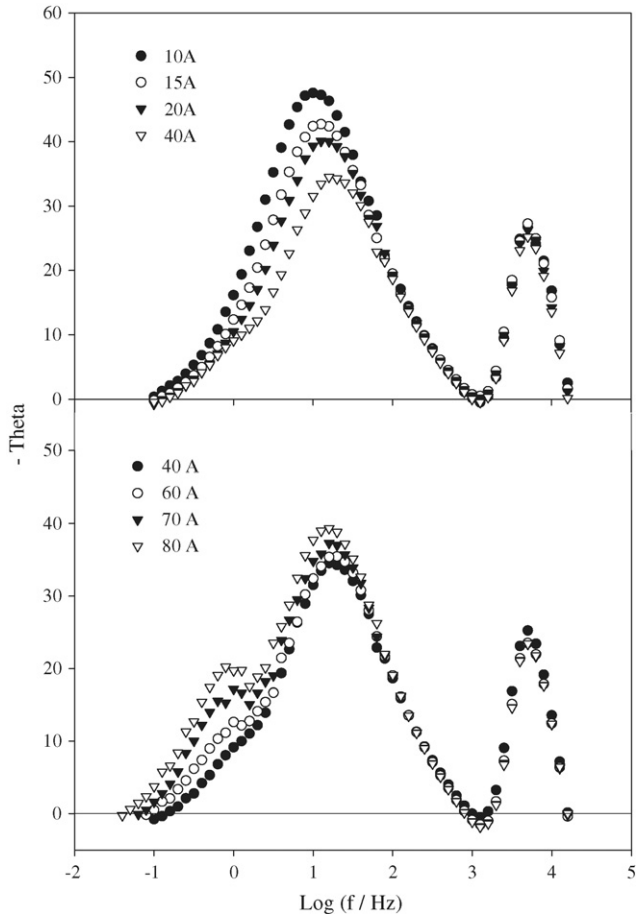

Fig. 12. Effect of air shortage on the Bode plots at 50 °C. The air flow rate was 20 L min^{-1}.

overpotentials is related to the water transport characteristics in the membrane. However, such explanations are not applicable in our experiments, which were controlled and dominated by the air supply, and were fully humidified at both the cathode and anode sides.

To summarize, the typical impedance spectra for the stack when operated at a fixed air flow rate included three arcs: the first arc at high frequency was associated with the structure of the MEAs or issues related to the measurement circuits, the second arc at medium frequency reflected the combination of an effective charge transfer resistance and a double-layer capacitance within the catalyst layer, and the third arc at low frequency related to the mass transport limitations caused by shortage of air supply. The medium and low frequency arcs correspond to the two relaxation times (i.e., charge transfer and mass transfer). In this case, without taking into account the high frequency feature, the equivalent circuit of the stack can also be presented as Fig. 3b.

If the stack is operated at a fixed hydrogen flow rate of 2 L min^{-1}, and the air inlet remains at a constant stoichiometry of 2.5, the impedance spectra will show the effect of hydrogen shortage on the Nyquist plots, as illustrated in Fig. 13a and b. At 30 °C, over the current range of 20–90 A, with increasing current, the kinetic loop becomes smaller. This is in accordance with the previous results. However, when the current reaches

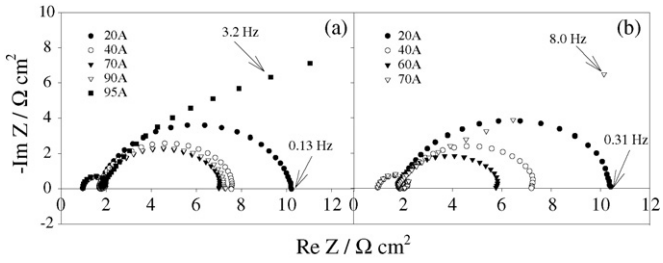

Fig. 13. Effect of hydrogen shortage on the Nyquist plots: (a) 30 °C and (b) 50 °C. The hydrogen flow rate was 2 L min^{-1}.

95 A, the complete loop cannot be detected, and the stack voltage decreases dramatically below 1 V. Similarly at 50 °C, over the current range of 20–60 A, with increasing current, the kinetic loop reduces. When the current reaches 70 A, the stack loses its normal function. From Fig. 13a and b, the additional third arcs did not appear because of the hydrogen shortage as they did in the case of air shortage. This is due to the fast reaction speed of hydrogen oxidation so that the spectrum mostly represents the cathode ORR behavior. This is also a proof that the small high frequency loops have nothing to do with the behavior of hydrogen oxidation because they remain stable even when there is a lack of hydrogen supply. In addition, shortage of hydrogen can be seen to be more dangerous than shortage of air. Once the shortage of hydrogen occurs, the stack is not able to perform, whereas in the case of air shortage, the performance drops gradually.

3.4. Humidity effect

At 30 °C, the spectra of the humidification cut-off at the cathode or the anode do not display big differences. But with increasing temperature, the effect becomes more and more significant. Fig. 14 shows the effect of cutting off the humidification at the cathode or the anode side at 50 A and 50 °C. The cut-off of anode humidification does not affect the spectra too much compared with the cut-off in cathode humidification. Dehydration of the anode also brings about a substantial increase of cathode impedance because a dry anode

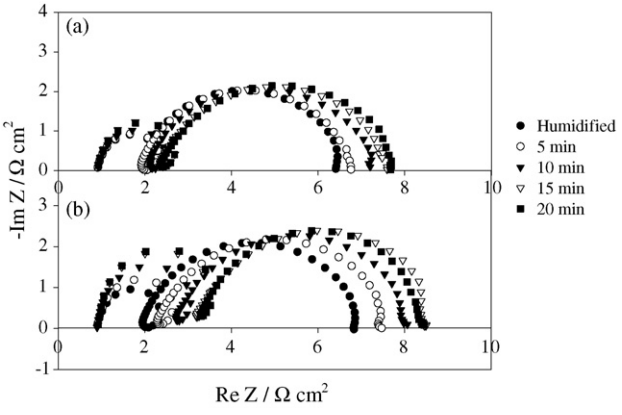

Fig. 14. Transients of the impedance spectra after interruption of the humidification at 50 °C. Initial state is humidified. Cutting off of: (a) anode humidification and (b) cathode humidification.

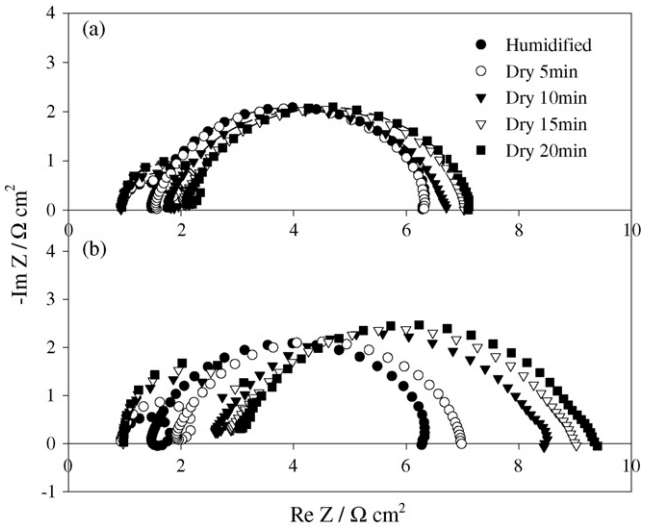

Fig. 15. Transients of the impedance spectra after interruption of the humidification at 70 °C. Initial state is humidified. Cutting off of: (a) anode humidification and (b) cathode humidification.

pulls water away from the cathode across the membrane, which make it hard to keep the cathode well hydrated [16]. The same phenomenon is also observed at 70 °C, shown in Fig. 15.

During the measurements, the high frequency arc, which is nearly independent of current, was found to grow as a result of the increase of the high frequency intercept of the kinetic loop. This can be observed in the humidification cut-off at either the cathode or the anode side, seen in both Figs. 14 and 15. As we know, the high frequency intercept on the real impedance axis of the kinetic loop is associated with membrane resistance. In fact, this intercept of the kinetic loop represents the total ohmic resistance of the cell, which can be expressed as a sum of the contributions from uncompensated contact resistance and ohmic resistance of the cell components such as the membrane, catalyst layer, backing layer, end plate, as well as the contact resistance between each of them [44]. Among these, bulk membrane resistance is the largest, and is strongly dependent on the hydration state of the membrane.

The measurement of membrane resistance gives important information on water management, which is a crucial issue for the successful operation of a PEM fuel cell. The conductivity of the membrane in a PEMFC is directly related to its water content, which depends on: (1) the water carried by the humidified reactant gases; (2) the water generated at the cathode; (3) the electro-osmotic drag, i.e., water carried by the protons from the anode to the cathode [11]; (4) the water diffusion. Therefore, the significant increase of membrane resistance after cutting off the humidification results from the lack of water carried by the reactant gases, and with a significant drop in the water concentration at the interface. Consequently, ionomer shrinkage may occur, reducing both the surface contact of the catalyst with the ionomer and the proton conductivity of the ionomer [45].

By fitting the kinetic loop, the diameter of the arc was found to increase slightly with time after cutting off humidification in both anode and cathode sides, seen in Table 1. It indicates that the lack of sufficient humidification of the reactant gases brings

Table 1
The diameters of the kinetic loops before and after interruption of the humidification at both cathode and anode sides

	Fitting diameters (Ω cm^2)			
	50 °C		70 °C	
	Cathode, dry	Anode, dry	Cathode, dry	Anode, dry
Humidified	5.1467	5.1565	5.1672	4.7145
5 min	5.184	5.0007	5.3962	4.8382
10 min	5.9024	5.0703	5.6123	5.2519
15 min	6.0598	5.1503	5.7188	5.2836
20 min	6.2418	5.2224	5.7304	5.5209

about cell performance losses because of an increase in the membrane resistance, and an increase of the interfacial impedance for ORR reflected by the increase of the overall diameter of the impedance loop [44].

As stated above, water transport in the membrane plays an important role in establishing the polarization behavior of polymer electrolyte fuel cells. Water content at the interface contributes to the transport of the involved species in many different ways. On the one hand, dehydration of the electrodes brings about a substantial increase of the stack impedance, resulting in stack performance loss. On the other hand, an extremely high water level can block oxygen transport, and the increased water concentration due to the water generation at the cathode can directly affect the ORR kinetics and also contribute indirectly to the state of contact between the Pt catalyst and the ionomer.

4. Conclusion

The EIS of a 500 W Ballard Mark V PEM fuel cell stack was measured successfully with the combination of a FuelCon test station, TDI loadbank, and Solartron 1260 in the galvanostatic mode. At low currents, typical spectra contained two semicircular loops. The low frequency loop corresponded to the charge transfer process of the ORR and the high frequency loop was associated with the internal ohmic resistance and the contact capacitance in the granular electrode structure of the MEAs or issues related to the measurement circuits. With increasing current in the low current range, the diameter of the low frequency arc (associated with charge transfer) decreased, thereby reflecting the increase in the driving force for the interfacial oxygen reduction process. Beyond 80 A, the kinetic loop started to distort and increase as the current increased due to mass transfer limits.

The effects of temperature, flow rate, and humidity on the stack performance were investigated. With increasing temperature, the diameter of the kinetic loop was observed to decrease. This is due to the slow ORR process at low temperature. When the stack is operated at a fixed air flow rate, a third low frequency arc grows, and with increasing current, the low frequency arcs become larger and larger due to the shortage of air. The shortage of hydrogen does not display an additional frequency arc in the spectra, but it is more dangerous than the shortage of air. At 30 °C, the humidification cut-off at either the cathode or anode does not show a big difference. But with increasing temperature,

the effect becomes more and more pronounced, and the cut-off of anode humidification does not affect the spectra as much as the cut-off in cathode humidification.

The high frequency intercept of the kinetic loop changes with temperature, and small differences can be observed between different currents. The investigation of the temperature and current dependence of the high frequency intercept of the kinetic arc is under way. Our future work will also include the EIS diagnosis on individual cells of the 500 W PEM fuel cell stack.

Acknowledgement

The authors gratefully acknowledge the National Fuel Cell program of National Research Council for supporting this project.

References

[1] C. Brunetto, G. Tina, G. Squadrito, A. Moschetto, in: M. Matijasevic, B. Pejcinovic, Z. Tomsic, Z. Butkovic (Eds.), Proceedings of the 12th IEEE Mediterranean Electrochemical Conference, vol. 3, Piscataway, NJ, 2004, pp. 1045–1050.
[2] G. Li, P.G. Pickup, J. Electrochem. Soc. 150 (2003) C745–C752.
[3] N. Wagner, J. Appl. Electrochem. 32 (2002) 859–863.
[4] J.-D. Kim, Y. Park, K. Kobayashi, M. Nagai, M. Kunimatsu, Solid State Ionics, Diffusion React. 140 (2001) 313–325.
[5] N. Wagner, E. Gulzow, J. Power Sources 127 (2004) 341–347.
[6] J.M. Song, S.Y. Cha, W.M. Lee, J. Power Sources 94 (2001) 78–84.
[7] Q. Guo, M. Cayetano, Y. Tsou, E.S. De-Castro, R.E. White, J. Electrochem. Soc. 150 (2003) A1440–A1449.
[8] E. Antolini, L. Giorgi, A. Pozio, E. Passalacqua, J. Power Sources 77 (1999) 136–142.
[9] S. Ahn, B.J. Tatarchuk, in: W.W. Schertz, R.H. Hill (Eds.), Proceedings of the 25th Intersociety Energy Conversion Engineering Conference, vol. 3, New York, 1990, pp. 287–292.
[10] B. Andreaus, A.J. McEvoy, G.G. Scherer, Electrochim. Acta 47 (2002) 2223–2229.
[11] T.J.P. Freire, E.R. Gonzalez, J. Electroanal. Chem. 503 (2001) 57–68.
[12] F.N. Büchi, G.G. Scherer, J. Electrochem. Soc. 148 (2001) A183–A188.
[13] H.A. Abaoud, M. Ghouse, K.V. Lovell, G.N. Al-Motairy, J. New Mater. Electrochem. Syst. 6 (2003) 149–155.
[14] C. Wang, Z.Q. Mao, J.M. Xu, X.F. Xie, J. New Mater. Electrochem. Syst. 6 (2003) 65–69.
[15] S.Y. Cha, W.M. Lee, J. Electrochem. Soc. 146 (1999) 4055–4060.
[16] T.E. Springer, T.A. Zawodzinski, M.S. Wilson, S. Gottesfeld, J. Electrochem. Soc. 143 (1996) 587–599.
[17] T. Abe, H. Shima, K. Watanabe, Y. Ito, J. Electrochem. Soc. 151 (2004) A101–A105.
[18] T.E. Springer, T.A. Zawodzinski, M.S. Wilson, S. Gottesfeld, in: S. Gottesfeld, G. Halpert, A. Landgrebe (Eds.), Proton Conducting Membrane Fuel Cells, The Electrochemical Society Proceedings Series, Pennington, NJ, 1995, pp. 137–151.
[19] J.D. Halla, M. Mamak, D.E. Williams, G.A. Ozin, Adv. Funct. Mater. 13 (2003) 133–138.
[20] M. Ciureanu, M. Badita, J. New Mater. Electrochem. Syst. 6 (2003) 163–168.
[21] H.C. Young, G.S. Yong, C.C. Won, I.W. Seong, S.H. Hak, J. Power Sources 118 (2003) 334–341.
[22] R. Halseid, P.J.S. Vie, R. Tunold, J. Electrochem. Soc. 151 (2004) A381–A388.
[23] M. Ciureanu, J. Appl. Electrochem. 34 (2004) 705–714.
[24] S. Slade, S.A. Campbell, T.R. Ralph, F.C. Walsh, J. Electrochem. Soc. 149 (2002) A1556–A1564.
[25] F. Damay, L.C. Klein, Solid State Ionics, Diffusion React. 162–163 (2003) 261–267.
[26] A. Sen, K.E. Leach, R.D. Varjian, in: D.H. Doughty, B. Vyas, T. Takamura, J.R. Huff (Eds.), Materials for Electrochemical Energy Storage and Conversion—Batteries, Capacitors and Fuel Cells, Materials Research Society Symposium Proceedings Series, Philadelphia, PA, 1995, pp. 157–162.
[27] R.F. Suva, M. De-Francesco, A. Pozio, J. Power Sources 134 (2004) 18–26.
[28] B. Andreaus, G.G. Scherer, Solid State Ionics, Diffusion React. 168 (2004) 311–320.
[29] M. Ciureanu, H. Wang, J. New Mater. Electrochem. Syst. 3 (2000) 107–119.
[30] J.D. Kim, Y. Park, K. Kobayashi, M. Nagai, J. Power Sources 103 (2001) 127–133.
[31] M. Ciureanu, H. Wang, J. Electrochem. Soc. 146 (1999) 4031–4040.
[32] J.P. Diard, N. Glandut, B. Le-Gorrec, C. Montella, J. Electrochem. Soc. 151 (2004) A2193–A2197.
[33] G. Bender, M.S. Wilson, T.A. Zawodzinski, J. Power Sources 123 (2003) 163–171.
[34] D.J.L. Brett, S. Atkins, N.P. Brandon, V. Vesovic, N. Vasileiadis, A. Kucernak, Electrochem. Solid-State Lett. 6 (2003) A63–A66.
[35] P. Godea, F. Jaouen, G. Lindbergh, A. Lundblad, G. Sundholm, Electrochim. Acta 48 (2003) 4175–4187.
[36] F. Jaouen, G. Lindbergh, K. Wiezell, J. Electrochem. Soc. 150 (2003) A1711–A1717.
[37] F. Jaouen, G. Lindbergh, G. Sundholm, J. Electrochem. Soc. 149 (2002) A437–A447.
[38] J. Ihonen, F. Jaouen, G. Lindbergh, A. Lundblad, G. Sundholm, J. Electrochem. Soc. 149 (2002) A448–A454.
[39] V.A. Paganin, C.L.F. Oliveira, E.A. Ticianelli, T.E. Springer, E.R. Gonzalez, Electrochim. Acta 43 (1998) 3761–3766.
[40] T. Romero-Castanon, L.G. Arriaga, U. Cano-Castillo, J. Power Sources 118 (2003) 179–182.
[41] A. Fischer, J. Jindra, H. Wendt, J. Appl. Electrochem. 28 (1998) 277–282.
[42] M. Ciureanu, R. Roberge, J. Phys. Chem. B 105 (2001) 3531–3539.
[43] M.L. Perry, J. Newman, E.J. Cairns, J. Electrochem. Soc. 145 (1998) 5–15.
[44] F. Lu, B. Yi, D. Xing, J. Yu, Z. Hou, Y. Fu, J. Power Sources 124 (2003) 81–89.
[45] J.M. Song, S.Y. Cha, W.M. Lee, J. Power Sources 94 (2001) 78–84.